Design and Experiment of a Novel High-Impact MEMS Ceramic Sandwich Accelerometer for Multi-Layer Target Penetration

MIN CUI [ID][1]**, YONG HUANG** [ID][2]**, JIAN LI** [ID][1]**, AND MING MENG** [ID][1]

[1] Shanxi Key Laboratory of Information Detection and Processing, North University of China, Taiyuan 030051, China
[2] Shanghai Institute of Aerospace Control Technology, Shanghai 201109, China

Corresponding author: Min Cui (cmcm_1980930@163.com)

ABSTRACT The output signal of traditional cantilever accelerometers usually overlapping and tailing during the high-velocity penetration process. And the sensitivity of traditional cantilever accelerometers cannot satisfy the application of multi-layer target penetration, that process contains large length-to-diameter ratios and high velocities. This paper proposes a novel high-impact Micro-Electro-Mechanical-System (MEMS) ceramic sandwich accelerometer (HMCSA) for the measurement of penetration-overload signals. Firstly, the HMCSA structure was designed and its structure-sensitive model was established. Then, the filling material in HMCSA was selected and the structure was simulated in ANSYS/LS-DYNA software. After that, the structure MEMS processing was introduced and the monitoring system was designed. Finally, the multi-layer target penetration process was simulated and HMCSA was tested in lab environment. The experiment verified that the design and manufacture of HMCSA was correct, and HMCSA can detect 30 000g acceleration.

INDEX TERMS Penetration layer counting, cantilever accelerometer, signal overlapping, ceramic-plate-capacitor sensor.

I. INTRODUCTION

Micro-Electro-Mechanical-System (MEMS) inertial sensors improve obviously in this decade [1]–[4]. High-g accelerometers were employed in smart fuzes to obtain the dynamic signals of penetration during the layer-counting application. Usually, a small projectile with lower velocity has a better vibration attenuation, and it gains clearer layer-penetration characteristics. However, if a projectile with larger length-to-diameter ratio and higher velocity ($\geq$600 m/s), and the stress wave will lead the high-frequency acceleration oscillation inside the projectile. The amplitude of high-frequency oscillation signal increases rapidly and immerses the overload envelope signal of the multi-layer target penetration completely. And this phenomenon causes the overlap of overload signals from individual layers, which makes penetration layer counting technology unavailable [5].

The associate editor coordinating the review of this manuscript and approving it for publication was Md. Moinul Hossain [ID].

One of the most effective methods to solve the above-mentioned problem is to improve the compensation circuit and algorithm for error and noise signals [6]–[12]. Donoho proposed de-noising method through using wavelet thresholding, the method typically involves the decomposition of the target signals using appropriately selected wavelets. And then, the decomposed high-frequency signals are filtered by using pre-established threshold functions. After that, the signals were reconstructed to obtain de-noised signals [6]. This signal processing technique can be used to remove a portion of the high-frequency noises in the signals and improve the signal-to-noise ratio. However, in practice, the filtering process based on the insufficient frequency analysis of penetration signals, which causes the ineffective filtering of high-frequency signals from the penetration resistance. The ensemble empirical mode decomposition (EEMD) algorithm was applied in the extraction of the layer-penetration characteristics of penetration-acceleration signals in work [8]. However, this method is hard to be realized by the restriction of hardware. Work [9] proposed

a layer-counting algorithm by combining signals from an accelerometer and MEMS switch. The algorithm determines the layer-penetration characteristics of projectile penetration by separately combining the convolutional weighted signals of the accelerometer and MEMS switch using different window functions in the time domain. However, the algorithm was only verified by conducting a software simulation of the penetration of five-layer targets at a projectile velocity of 700 m/s. In work [10]–[11], the applicability of the algorithm for higher projectile velocities were certificated by using physical experiments. In general, the existing researches on the solution of the acceleration signal overlap problems are mainly focused on the improvement of the algorithms. And the algorithms usually extract of the overload envelope of the complex signals of multi-layer penetration using high-frequency filtering, modal decomposition, and overload threshold recognition. However, the algorithms are complex and off-line, and the parameters (such as the cut-off frequency, number of modal decompositions, and overload threshold for targets of different characteristics) are not self-adaptive. Fundamentally, the signal overlap problem is difficult to solve, and more reliable measurement data are required [13]–[18].

Traditionally, penetration signals are obtained using high-g MEMS accelerometers, which mostly have cantilever structures. This type of accelerometer offers the advantages of a high sensitivity and well-established manufacturing technologies. However, they cannot immediately stabilize at the balance position after the initiation of vibrations. Thus, for applications in fuzes with respect to multi-layer penetration, the accelerometer is not stabilize for the previous penetrated layer when the next layer is penetrated. This results in the overlap of overload signals for individual layers, in addition to the ineffective sensing of the penetrated layers.

This study focus on the solution of the signal overlap problem, and a novel high-impact MEMS ceramic sandwich accelerometer (HMCSA) is proposed to obtain the reliable penetration signal data. Compared with the normal cantilever accelerometers, HMCSA employs capacitive detection method and has higher vibration frequency. So, it can obtain high-frequency penetration signals effectively and the low-frequency interfering signals can be restricted by filter. Moreover, the larger stiffness helps HMCSA to return to the balance position more rapidly, which is better for multi-layer target penetration detection. Thereby, HMCSA solves the signal overlap problem and effectively prevents the signal tailing phenomenon [19].

II. HMCSA STRUCTURE DESIGN
A. HMCSA STRUCTURE WORKING PRINCIPLE
Usually, the input acceleration range of a round capacitive sensor structure is higher than a square capacitive structure with the same size. Thus, the pressure-sensitive plate and dielectric layer were designed as round. The common working principles of capacitive sensors include the variable polar

distance, variable area, and variable dielectric constant. Considering the high impact of projectile penetration, the capacitive sensor was designed as a variable-polar-distance type using a high-strength, impact-resistance, and high-hardness dielectric material, as shown in Figure 4. Here, t_g is the initial thickness of the dielectric layer, and t_m is the thickness of the upper polar plate (pressure-sensitive). When an external force acts on the upper polar plate, the entire capacitor-sensing element is deformed, which results in a change in its capacitance. Thus, the impact of the projectile results in a change in the polar distance, which leads to a change in the capacitance of the capacitive sensor.

The upper polar plate is the critical component of the capacitive structure, its dynamics characteristic is analyzed based on elastic thin plate material mechanics principle. The deformation of the upper plate under the external load can be classified into two types: large-deflection deformation and small-deflection deformation. Table 1 presents the application scopes of two deformation types.

TABLE 1. Theoretical application scopes of large- and small-deflection deformation.

Type of deformation	Scope of application
Large-deflection deformation	$W_{max} < 20\% \times$ thickness of thin plate
Small-deflection deformation	$W_{max} \geq 20\% \times$ thickness of thin plate

The small-deflection deformation of the upper polar plate varies linearly with impact penetration. The maximum deformation of the polar plate occurs in the middle part, and it is designated as W_{max}, as shown in Figure 1. The edges of the upper polar plate are fixed. Thus, W_{max} can be obtained by solving the following equation for round membranes with fixed edges:

$$W_{max} = 0.01146 \frac{P\pi^2 a^4 / 16 \left(1 - \sigma^2\right)}{Et_m^3} \qquad (1)$$

where, P is the pressure; a is the diameter of the upper polar plate; E is the modulus of elasticity of the upper polar plate; and σ is the Poisson ratio.
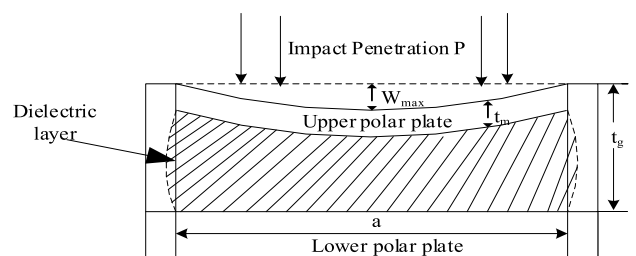
FIGURE 1. Schematic illustration of the capacitive sensor designed using a dielectric material.

For the large-deflection deformation, the tensile deformation of the upper polar plate cannot be neglected, and the deformation varies non-linearly with respect to the impact penetration. The initial capacitance of the capacitive sensor subjected to no external force, C_0, can be expressed as follows:

$$C_0 = \frac{\varepsilon_0 \varepsilon_r \pi a^2/4}{t_g} + \frac{\varepsilon_0 \varepsilon_r \pi/4 \left(a_r^2 - a^2\right)}{t_g} \quad (2)$$

where, ε_0 is the relative dielectric constant; ε_r is the relative dielectric constant of the dielectric material, and a_r is the diameter of the lower polar plate (fixed polar plate). The first term of the right side equation is the capacitance when the upper and lower polar plates have the equal area. When the upper and lower polar plates have the same shape and area, the second part on right side equation is the capacitance resulting from the edge effect of the upper and lower polar plates.

When the impact penetration inputs, the relationship between the variable capacitance and the maximum deflection of the upper polar plate can be expressed as follows:

$$C(P) = \frac{C_0}{\sqrt{\gamma}} \tanh^{-1}\left(\sqrt{\gamma}\right) \approx C_0\left(1 + \frac{\gamma}{3} + \frac{\gamma^2}{5}\right) \quad (3)$$

where

$$\gamma = \frac{W_{\max}}{t_g} \quad (4)$$

When $\left|W_{\max}/t_g\right| \ll 1$, C and P satisfy the following linear relationship:

$$
\begin{aligned}
C(P) &= C_0\left(1 + \frac{\gamma}{3}\right) = \frac{C_0}{3t_g}W_{\max} + C_0 \\
&= \frac{0.00214\pi C_0 a^4 \left(1 - \sigma^2\right)/4}{t_g E h^3}P + C_0 \quad (5)
\end{aligned}
$$

The above equation expresses that the upper polar plate capacitance caused by small-deflection deformation is approximately linearly with the input impact penetration, as shown in Figure 2.
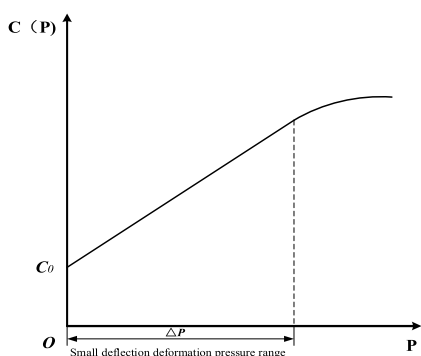

FIGURE 2. Characteristics curve of C(p) – P relationship.

Based on the above linear relationship between the HMCSA structure capacitance and input impact penetration,

the HMCSA structure sensitivity S can be expressed as:

$$S = \frac{\Delta C}{\Delta P} \quad (6)$$

where, ΔP is the variation of input impact penetration; ΔC is the variation of HMCSA structure capacitance. The above equation indicates that higher ΔC value for a steady ΔP results in a higher HMCSA structure sensitivity. Combining Equations (2) and (5), ΔC can be expressed as:

$$
\begin{aligned}
\Delta C &= C(P_1) - C(P_2) \\
&\approx C_0\left[\left(\frac{\gamma_1}{3} + \frac{\gamma_1^2}{5}\right) - \left(\frac{\gamma_2}{3} + \frac{\gamma_2^2}{5}\right)\right] \quad (7)
\end{aligned}
$$

The above equation expresses that the sensor sensitivity is determined by two parameters, namely, C_0 and γ; which are related to the HMCSA structure parameters. To improve the sensitivity of the sensor, the polar plates and dielectric material should be optimized. In addition, the effective area of the polar plates should be large enough, and the thickness of the dielectric layer should be as small as possible to make the HMCSA structure as small as possible.

B. SELECTION OF DIELECTRIC MATERIAL FOR THE CAPACITIVE SENSOR

The measurement accuracy of HMCSA structure can be improved under high-overload conditions by the following two steps:

First, the above equations express that thinner electric layer achieves higher structure sensitivity. But thinner layer decrease the structure strength, which results in the poor survival ability of the HMCSA structure under high-overload conditions.

Second, the dielectric material requires low Q value (quality factor), wide frequency response, and high strength characteristic. Usually, smaller deformation of the dielectric layer results in a wider measurement range, more rapid attenuation of structural vibration, and less possibility of signal overlapping.

The common dielectric materials used for wide-measurement-range capacitors include complex oxide ceramics, tempered glass, and mono-crystalline silicon. Table 2 presents a comparison of the parameters of the three different materials. The table reveals that ceramics have significantly higher moduli of elasticity than the other two materials, which means that the ceramic dielectric layer

TABLE 2. Comparison of the parameters of three dielectric materials.

Parameter description	Complex oxide ceramics	Tempered glass	Mono-crystalline silicon
Modulus of elasticity (GPa)	300	72	160
Moh's hardness	8.9	6.5	7

exhibits smaller deformation than other two materials. Moreover, ceramics material has higher hardness than the other two materials. A high-hardness dielectric material is required to ensure the linear output of the capacitive sensor, and a material with a high hardness typically has a high strength. Moreover, ceramics material almost does not have plastic deformation when subjected to quasi-static one-dimensional tensile stress, while the other two materials fracture and fail during the elastic deformation stage. This indicates that ceramics have very small extensibility. Ceramics material fails in the elastic deformation stage when subjected to quasi-static one-dimensional compression. Moreover, the ultimate compressive strength of ceramics material is significantly greater than their ultimate tensile strength. Thus, ceramics demonstrate non-symmetric mechanical performances under tensile and compressive conditions [30]. Since the HMCSA structure is for compressive-deformation applications, ceramics material is suitable for the dielectric layer.

Ceramics material is brittle that demonstrate a good physical-mechanical performance and completely different response characteristics under high-impact dynamic loads. Most of the ceramic dielectric layers of capacitive sensors for the measurement of high-impact dynamic loads use complex oxide ceramics such as aluminum nitride, zirconia, and alumina. Samples of the sensor were made with dielectric layers of different thicknesses using three different ceramics (aluminum nitride, zirconia, and alumina). The samples (with the polar plate of the same thickness) were then subjected to an impact test under the same conditions. Figure 3 presents the frequency response curves obtained from the impact test of the samples.
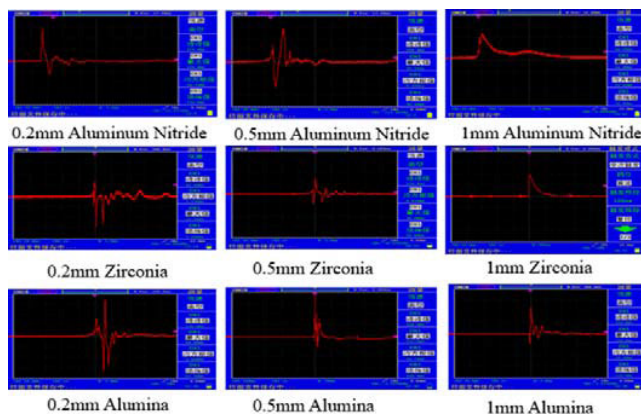

FIGURE 3. Results of high-impact test of sensor samples made with dielectric layers of different thicknesses using different materials.

Figure 3 reveals that, for all three ceramics materials, with an increase in the thickness of the dielectric layer, the Q value decreases, and the phenomenon of signal tailing improves. A comparison of the three different ceramics revealed that the 1-mm thick dielectric layer made with zirconia exhibited the smoothest attenuation among the dynamic response curves, wherein no oscillation attenuation was observed.

Thus, zirconia is the most suitable option for applications where a low Q value is desirable. Zirconia was finally selected as the dielectric material for the sensor.

C. HMCSA STRUCTURE OPTIMIZATION

In order to improve the sensitivity of HMCSA structure, the double-layered plate capacitor is designed with a chamber made using a dielectric material with a low Q value and wide response, two dielectric plates, and a conductive plate. This design contributes to the maximization of the penetration measurement sensitivity and the variation range of capacitance. The structure does not use elastic reinforcement for the chamber. This is to minimize the Q value of the structure and shorten the impact response time. The edges of the printed circuit board (PCB) were protected with fillers to buffer the impact, as shown in Figure 4. The damping coefficient of the sensor was adjusted by adjusting the thickness of the dielectric layer.

FIGURE 4. Schematic illustration of the capacitive sensor designed using a dielectric material.

D. DYNAMICS SIMULATION OF THE CAPACITIVE SENSOR

The ANSYS finite element analysis software was employed to verify the HMCSA structure dynamic characteristic. A high-G shock simulation was conducted using the by applying different impact loads (40,000 g, 100,000 g, 150,000 g, and 200,000 g) to HMCSA structure. Table 3 presents the maximum deformation and maximum equivalent stress obtained using a steady-state analysis.

TABLE 3. Comparison of the parameters of three dielectric materials.

Parameters Impact load	Maximum deformation (μm)	Maximum equivalent stress (MPa)
4×10^4 g	2.636	17.676
10×10^4 g	3.762	25.583
15×10^4 g	4.701	31.576
20×10^4 g	5.639	38.114

The ceramic dielectric layer fractures earlier than the metal (lead-silver alloy) polar plate when the capacitor is subjected to a high-overload impact that exceeds its structural strength. This is because zirconia is more brittle than the alloy. Therefore, a steady-state analysis of the structural strength of the sensor was conducted under the condition that the maximum

equivalent stress of the structure does not exceed the ultimate strength of zirconia (i.e., the structure does not fail). Previous research revealed that the ultimate strength of zirconia is 950 MPa. Thus, the structural strength of the capacitive sensor can satisfy this requirement.

To further demonstrate the excellent dynamic response characteristics of the capacitive sensor, a comparative analysis of its modal and instantaneous responses was conducted using the ANSYS software. Table 4 presents the material parameters of the capacitive sensor.

TABLE 4. Comparison of the parameters of three dielectric materials.

Parameter / Material	Density (g/cm^3)	Poisson ratio	Modulus of elasticity (GPa)
Zirconia	5.89	0.25	220
Lead-silver alloy	11.00	0.42	11.50

A gridded geometric model was established for the capacitor, as shown in Figure 5.
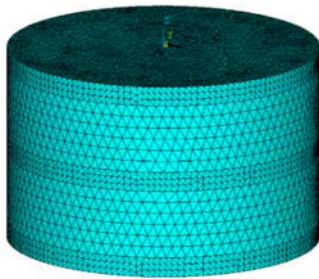
FIGURE 5. Schematic illustration of the finite element model for the capacitor.

The maximum acceleration of the penetrating projectile determined by the dynamic simulation, as presented previously, was 25,000 g. To ensure the structural integrity of the sensor, especially in the case wherein the high overload exceeds its measurement range, it is typically designed to bear a maximum impact acceleration (a_{max}) that is equal to the maximum impact acceleration that can be measured within its measurement range a_{max}, multiplied by a safety coefficient δ:

$$\overline{a_{\max}} = \delta \cdot a_{\max} \tag{8}$$

In this study, δ was set as 1.6. Thus, the finite element simulation of the two structures was conducted at an impact acceleration of 40,000 g. The simulation results were obtained to compare the response characteristics of the two structures.

The modal simulation was mainly conducted to obtain a clear description of the vibration characteristics of the sensor. The modal analysis was conducted using the modal analysis function available on the ANSYS software platform, with the extended mode set as 4. Figure 6 presents the results (four orders of mode) of the modal simulations of the double-layered plate capacitor.

TABLE 5. Vibration frequencies of the capacitor at different orders of mode.

Order of mode	1	2	3	4
Vibration frequency (kHz)	77.937	77.940	77.946	156.792

Table 5 presents the first vibration frequencies of the capacitor at different orders of mode.

The model analysis simulation results revealed that the natural frequency of the capacitor in the direction of the impact acceleration in the first-order mode was 77.940 kHz. The cut-off frequency of the spectral response due to the impact of the penetrating projectile was lower than 20 kHz. The nature frequency of HMCSA structure ω_0 should be 3-5 times higher than the cut-off frequency of the target signal. This is to ensure the accuracy of the dynamic measurement. Thus, the double-layered plate capacitor can satisfy the requirement of no measurement distortion.

The excellent response characteristics of the capacitive sensor to step signals under high impact conditions were further verified by conducting an instantaneous dynamics simulation. Figure 8 presents the results of the instantaneous simulation under the high-impact acceleration of 40,000 g, as shown in Figure 6.

The instantaneous response curve of the sensor yielded a response time of 20 μs. Thus, the capacitive sensor satisfies the requirement of a short dynamic response time for penetration layer counting. The instantaneous response curve of the sensor exhibited a gradual increase, the curve was smooth, and the signal tailing phenomenon was not observed. Thus, the sensor can effectively prevent the signal overlapping phenomenon.

III. IMPACT PENETRATION MEASUREMENT PRINCIPLE SIMULATION

The dynamics of the projectiles that penetrated multi-layer targets were simulated in finite element simulation environment. And the simulation results are utilized to establish the physical experiment platform for HMCSA.

The real projectiles have very complex internal structures; thus, in the simulation, they were simplified as solid structures. Testing loads were then applied in the sensor structure simulation according to the results of the projectile penetration simulation. The penetration model was designed based on the following three assumptions with respect to the target and projectile:

(1) The target and projectile are made of uniform, continuous, and isotropic materials, and the projectile is a rigid model. The target is an infinite square plate, and the target and projectile are not influenced by the boundary effect and initial stress.

(2) The projectile is perpendicular to the surface of the target, and the effect of gravity is negligible.
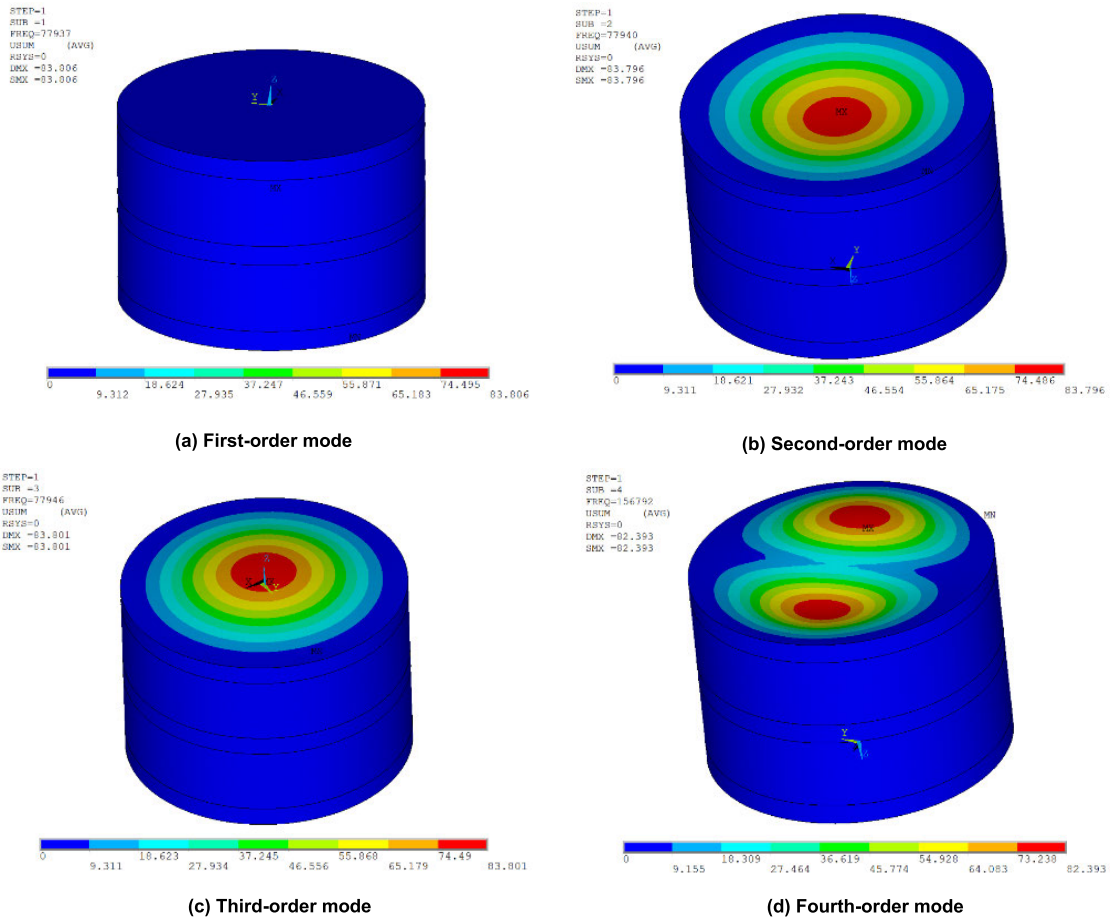
(a) First-order mode

(b) Second-order mode

(c) Third-order mode

(d) Fourth-order mode

FIGURE 6. Modal simulation of the structure of the double-layered plate capacitor.
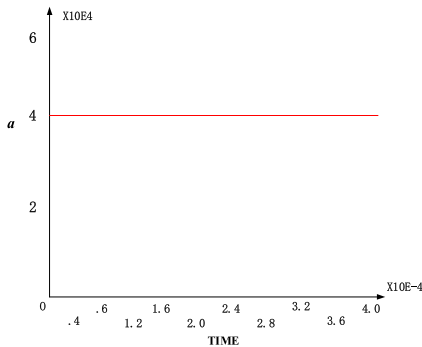

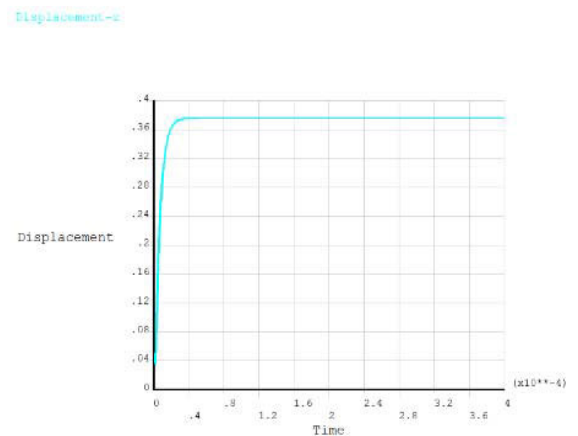**FIGURE 7.** High-impact acceleration signal.

FIGURE 8. Instantaneous response of the capacitive sensor.

(3) The entire penetration process is adiabatic. The effect of air resistance and projectile vibration is negligible.

Figure 9 presents the geometric model of the penetration. The penetration test is computed using the Lagrange method. The diameter and length of projectile are 2.6 cm and 3.9 cm respectively. The head of the projectile is hemispheric, with a diameter of 2.6 cm. The penetration model is gridded using Solid 164, which is a three-dimensional solid element. The grids in the area of the direct projectile-target

interaction are refined. The boundary conditions are defined as non-reflecting, to simulate the semi-infinite target. The projectile-target contact is simulated as a surface-to-surface contact using *CONTACT_ERODING_SURFACE_TO_SURFACE algorithm [20]. This is a two-way contact
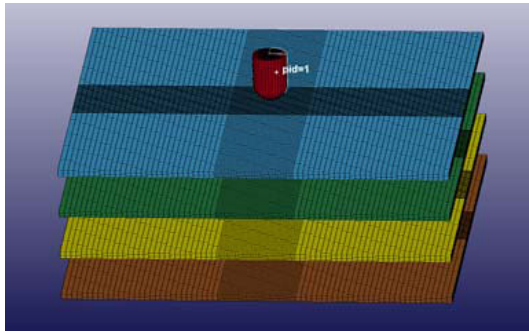
FIGURE 9. Geometric model of projectile penetrating a multi-layer target.

algorithm recommended in LS-DYNA for analyzing metal penetration and compression deformation.

The projectile is simulated as a rigid-elastic model. The material model is defined as ∗MAT_JOHNSON_ COOK for the description of its constitutive relationship [21]. The Johnson Cook model is a classical metal material numerical simulation model, and the simulation results are closer to the physical test. Table 6 presents the detailed parameters of the material.

TABLE 6. Material parameters of the projectile.

mid	RO	G	E	PR	PC	SPALL	D1
1	7.83	0.77	2.2	0.3	-9	3.0	5.0
A	B	N	C	M	TM	TR	EPSO
0.00792	0.0051	0.26	0.014	1.03	1793	294	10^{-6}
CP	EFMIN						
4.77×10^{-6}	10^{-6}						

The four-layer concrete target plate adopts the ∗MAT_RHT model, which can reflect the response of concrete under high pressure and strong strain more clearly. The material parameters of each concrete target except the material number are the same, and the detailed parameters of the specific materials are shown in Table 7 below.

TABLE 7. Material parameters of the target.

mid	RO	SHEAR	ONEMPA	EPSF	B0	B1
2	2.314	0.139	1.E-6	1.0	1.22	1.22
A	N	FC	FS*	FT*	Q0	B
1.60	0.610	3.50E-4	0.18	0.10	0.6805	0.0105
EOC	EOT	EC	ET	BETAC	BETAT	PTF
3E − 11	3E − 12	3E + 22	3E + 22	0.032	0.0360	0.001
GAMMA	A1	A2	A3	PEL	PCO	NP
0.0	0.3527	0.3958	0.0904	2.33E-4	0.06	3.0

The unit of the simulation was cm-g-us. The initial velocity of the projectile was set as 1,300 m/s, and the simulation time

is set as 180 μs. The specific boundaries and initial conditions are shown in Table 8:

TABLE 8. Numerical simulation initial condition.

Initial velocity of the projectile （m/s）	Projectile material	Target material	Fixing method around the target
1300m/s	A30 steel	Concrete	Fully fixed

After completing the pre-treatment and loading, the K document derived from the previous step was processed using the ANSYS solver, with the outcome exported as a d3plot file. The file was imported into the LS-PREPOST program for a visual observation of the deformation, stress [22], and strain during the penetration of the target by the projectile. The time curves of the penetration velocity and acceleration of the projectile were then directly exported from the program. The parameters of the projectile such as the maximum penetration acceleration, overload strength interval, and shortest inter-layer flying time of the projectile were then obtained, as shown in Figures 10 and 11.

The curve shown in Figure 11(b) is very smooth, given that the vibration within the projectile was neglected, and the signal consists of only the rigid velocity of the penetrating projectile, which excludes the harmonics within the projectile. It should be noted that this is an idealized signal curve for the sensor based on a simplification of the actual complex penetration process. However, noise does not have a significant impact on the amplitude of signals. It is therefore reasonable to use the maximum acceleration of the penetrating projectile shown in Figure 11(b) as the a priori condition for the sensor structure simulation. Table 9 presents the parameters of the motion of the penetrating projectile motion.

IV. HMCSA MANUFACTURE
A. HMCSA Structure Processing
Some key processing technology during HMCSA structure processing employed MEMS technology [23], and Figure 12 presents the manufacturing process of the HMCSA Structure, and the processing steps are:

Step 1: Machine two zirconia plates to dimensions in accordance with the design specifications using mechanical machining.

Step 2: Screen-print conductive Pd-Ag ink on the two ceramic plates using thick-film technology. The resulting products are used as the polar plates of the capacitor.

Step 3: Assemble the two ceramic plates into a two-layer plate capacitor. Pre-sinter the capacitor under exposure to an infrared lamp at room temperature for 30 min to prevent the structure from bubbling. Sinter the capacitor in a tunnel furnace at a high temperature of 850 °C. This is to enable the recrystallization of the metal palate molecules, thereby improving the structural strength of the capacitor. Thereafter, vacuum-cool the capacitor at room temperature for 1.5 h.
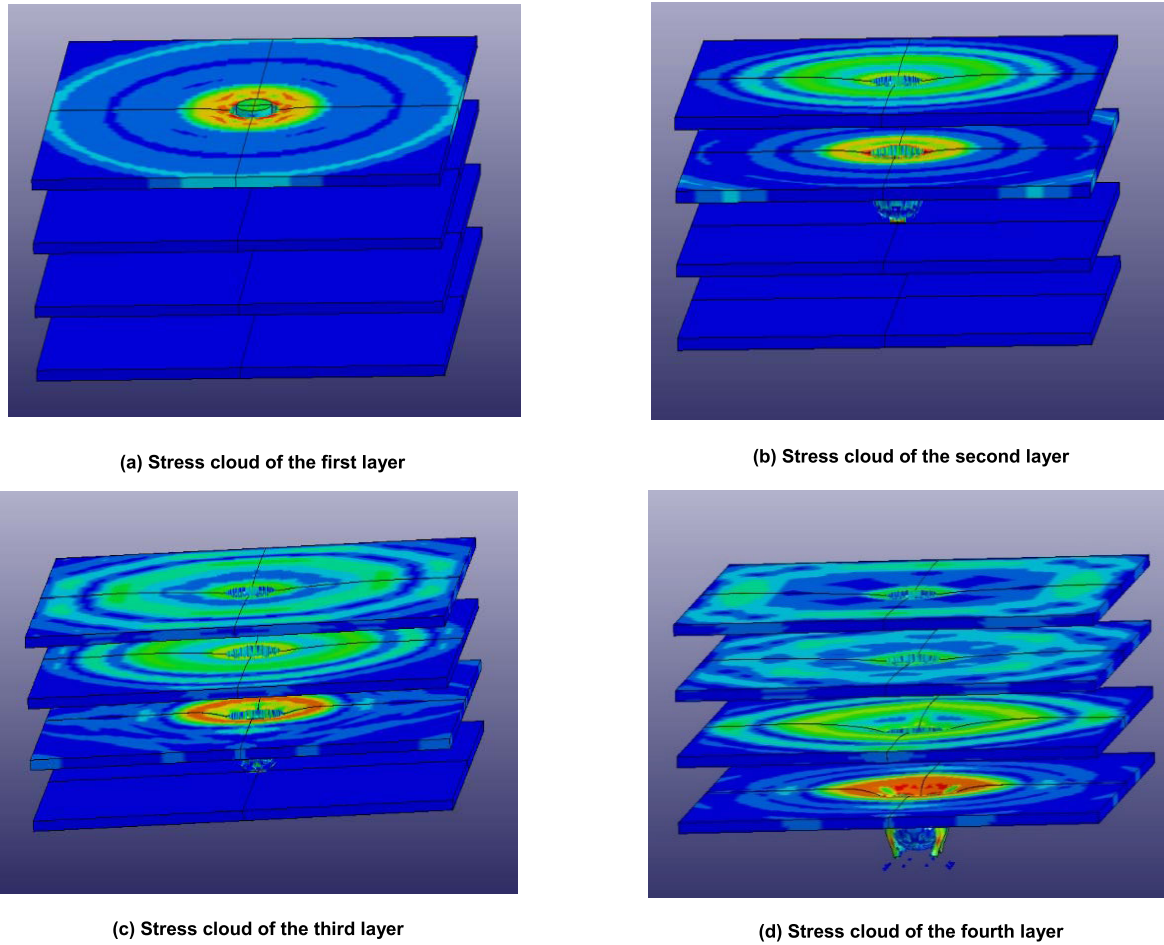
(a) Stress cloud of the first layer

(b) Stress cloud of the second layer

(c) Stress cloud of the third layer

(d) Stress cloud of the fourth layer

FIGURE 10. Stress clouds of the projectile penetrating the multi-layer target.

TABLE 9. Parameters of the penetrating projectile motion.

Penetration parameter/value	Maximum penetration velocity (g)	Time for penetrating an individual layer (μs)
First layer	18,537	25
Second layer	23,865	30
Third layer	25,000	25
Fourth layer	16,726	23

Step 4: Remove the two-layer plate capacitor, and link the three polar plates with leads using metal. This completes the manufacturing process for the capacitive sensor.

B. HMCSA MONITORING CIRCUIT SYSTEM

The measurement circuit system of HMCSA consists four parts, as shown in Figure 13. In capacitance detection part, tiny capacitance detection technology is employed to improve the signal noise rate of HMCSA structure [24].

The major functional relationship between the four parts is as follows. The conditioning circuit coverts the analog capacitance output from the sensor to voltage analog signals that can be received by the analog to digital converter (ADC) signal acquisition circuit. The signal acquisition circuit converts the voltage analog signals into digital values that can be recognized by the processor. The field-programmable field array (FPGA) control circuit carries out the real-time processing of the penetration data. The flash memory circuit stores the signals acquired by the signal acquisition circuit. The stored signals can then be exported for post-mission data treatment. The flash memory circuit can also store low-pass filtering coefficient program codes pre-programmed by the FPGA. The codes can be retrieved by the FPGA for the in-mission processing of penetration signals.

Figure 14 and 15 present the operation principle of the PCB for the measurement circuit system of the sensor.

## V. SEMI-PHYSICAL TEST OF THE MULTI-LAYER TARGET PENETRATION SENSOR
A. LABORATORY TEST

As previously detailed, the structural integrity of the double-layered plate-capacitor sensor was verified by conducting a theoretical analysis and finite element simulation analysis. The PCB was designed, and samples of the sensor were
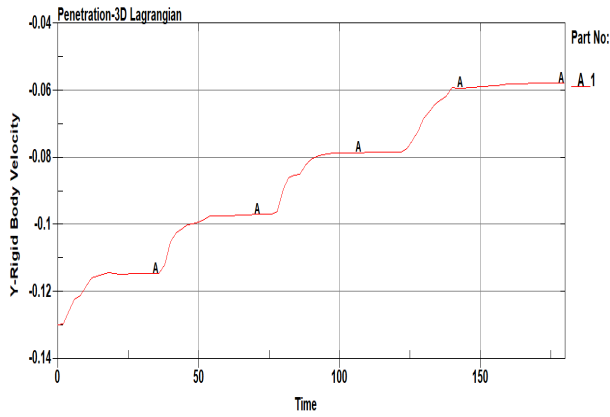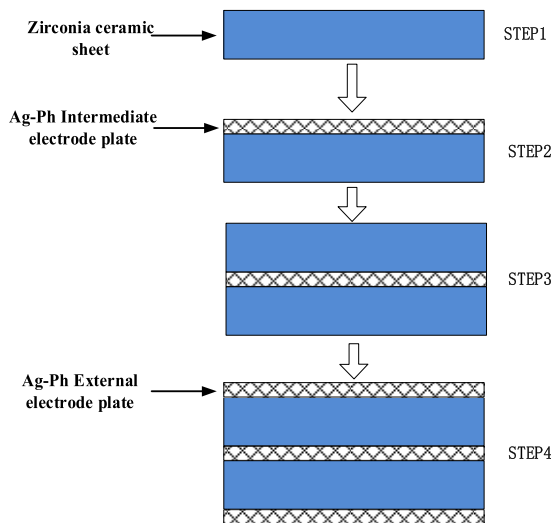
(a) Vertical velocity–time curve of the projectile
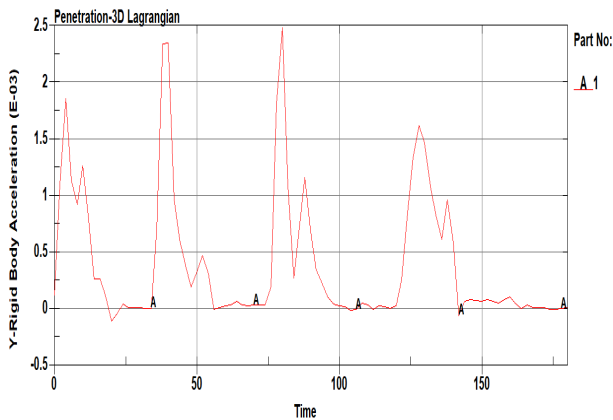
(b) Vertical acceleration–time curve of the projectile

FIGURE 11. Time curves of the velocity and acceleration of the projectile penetrating the multi-layer target.

**FIGURE 12.** Manufacturing process of the HMCSA structure.

manufactured using the embedding technology. This section describes the performance test of the sensor. In general, the most direct test method involves the installation of the
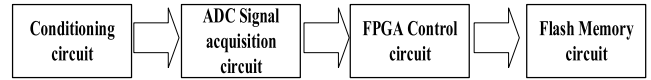
FIGURE 13. Overall framework of the measurement circuit system.

FIGURE 14. Front-side of the PCB for the sensor measurement circuit system.
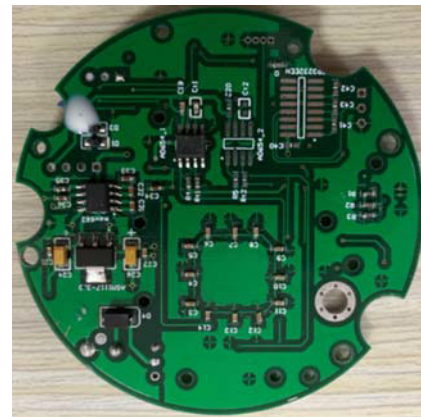
FIGURE 15. Back-side of the PCB for the sensor measurement circuit system.

sensor in a projectile, and then testing it within a target range. However, the target range test has the disadvantages of a high cost and long cycle time. Moreover, the integrity of the tested projectile is uncertain. Thus, the test may have to be carried out multiple times.

A hydraulic impact tester is commonly used to conduct high-impact tests on sensors in the laboratory environment. The hydraulic impact tester (SY10-100, Dongling, China) used in this study is as shown in Figure 16. The tester offers the following advantages:

1) Can produce high-impact acceleration
2) Easy operation
3) Can test the structural strength of sensor samples

To simply demonstrate the excellent impact response characteristics of the capacitive sensor in comparison with those of the MEMS accelerometers, these two types of sensors were

FIGURE 16. Hydraulic impact tester used in this study.

FIGURE 17. Double-layered plate-capacitor sensor.

FIGURE 18. Accelerometer used in this study.

FIGURE 19. Output signals of the capacitive sensor.

FIGURE 20. Output signals of the accelerometer.

tested separately for their dynamic output characteristics at the same impact acceleration using the abovementioned hydraulic impact tester. Figures 17 and 18 present images of the capacitive sensor and a MEMS accelerometer. A 7270A-200K uniaxial accelerometer (7270A-200K, Endevco, Germany) with a measurement range of 150,000 g was selected for the test. The designed capacitive sensor has a response sensitivity of 580mV/g through centrifugal calibration technology.

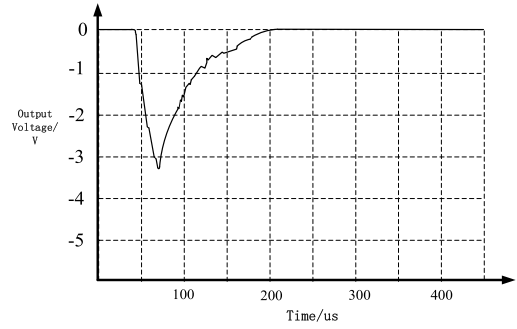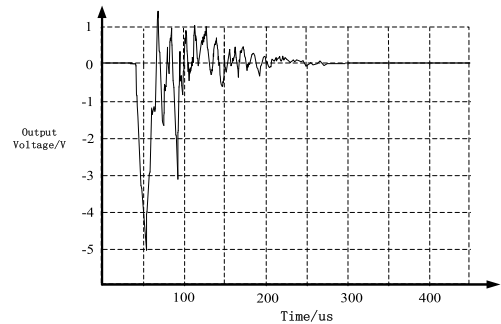In this test, the SY10-100 hydraulic impact test rig is used for sensor calibration. The system includes four parts: the front impact head, the hydraulic excitation system, the upper machine impact control system and the acquisition system of the sensor under test. The parameters such as the impact acceleration and the impact time of the impact head are controlled by the upper computer to simulate the force of the internal acceleration sensor when the projectile penetrates the concrete target.

And the effective measurement range is 0-200000g. For target range tests, the targets typically have thicknesses of 0.2–0.3 m and are built using C30 concrete. At an initial penetration velocity of 800 m/s, the peak overload acceleration of the projectile is typically within the range of 20, 000–30, 000 g. The penetration requires approximately 300 μs. Moreover, the employed hydraulic impact tester can produce a maximum acceleration pulse width of 400 μs and a maximum impact acceleration of 50,000 g. Thus, the tester can simulate the penetration of single-layer targets.

The tester was hinged to a vibration machine. Figures 19 and 20 present the dynamic responses of the capacitive sensor and the MEMS accelerometer, respectively, tested under an impact acceleration of 30,000 g. The relevant boundaries and initial conditions are shown in the following table 10:

B. TESTING RESULTS ANALYSIS

When the dynamic signal output by the designed sensor is less than 5%, the output signal is considered to converge. The testing results revealed that the output voltage signals

TABLE 10. Test related boundary condition.

Pulse duration (μs)	Pulse peak (g)	Sensor fixing method	Ambient temperature
50	30000	Fixed hinge mounting	70℃±5℃

of the capacitive sensor exhibited no oscillation attenuation, whereas the output voltage signals of the accelerometer exhibited significant oscillation attenuation. A comparison of the signals of the two sensors revealed that the captive sensor demonstrated a weaker signal tailing effect.

VI. CONCLUSIONS

This paper presents a novel high-impact MEMS ceramic sandwich accelerometer (HMCSA) for multi-layer target penetration. A double-layered plate-capacitor HMCSA structure was designed using zirconia as the dielectric material. Simulations of the modal and instantaneous responses of the HMCSA was conducted using ANSYS software. Then, the penetration of the multi-layer hard target was analyzed, and the model for a projectile penetrating a four-layered target was established using LS-DYNA software. The manufacture processing for HMCSA structure was introduced. The HMCSA sensor was designed with a measurement circuit system that consisted of a conditioning circuit, ADC signal acquisition circuit, FPGA control circuit, flash memory circuit, and power source circuit. Moreover, the circuit system outputs analog voltage signals, can process digital data, and then store the processing results in the flash chip for post-mission data treatment. The experiments were arranged in the final part and the results proved that HMCSA worked well.

REFERENCES

[1] A. D'Alessandro, S. Scudero, and G. Vitale, "A review of the capacitive MEMS for seismology," *Sensors*, vol. 19, no. 14, p. 3093, 3093.

[2] H. Cao, H. Li, X. Shao, Z. Liu, Z. Kou, Y. Shan, Y. Shi, C. Shen, and J. Liu, "Sensing mode coupling analysis for dual-mass MEMS gyroscope and bandwidth expansion within wide-temperature range," *Mech. Syst. Signal Process.*, vol. 98, pp. 448–464, Jan. 2018.

[3] J. Wilde, "30 years of sensors' assembly and packaging 1988 to 2018," *Sensors Mater.*, vol. 30, no. 9, pp. 1935–1945, Sep. 2018.

[4] H. Cao, R. Xue, Q. Cai, J. Gao, R. Zhao, Y. Shi, K. Huang, X. Shao, and C. Shen, "Design and experiment for dual-mass MEMS gyroscope sensing closed-loop system," *IEEE Access*, vol. 8, pp. 48074–48087, 2020, doi: 10.1109/ACCESS.2020.2977223.

[5] F. Li, D. Zuo, and L. Hu, "Overview on test technology of fuze," *Amer. Inst. Phys. Conf. Ser.*, 2017.

[6] D. Donoho, "50 years of data science," *J. Comput. Graph. Statist.*, vol. 26, no. 4, pp. 745–766, 2017.

[7] H. Cao, Y. Liu, Y. Zhang, X. Shao, J. Gao, K. Huang, Y. Shi, J. Tang, C. Shen, and J. Liu, "Design and experiment of dual-mass MEMS gyroscope sense closed system based on bipole compensation method," *IEEE Access*, vol. 7, pp. 49111–49124, 2019.

[8] S. Gaci, "A new ensemble empirical mode decomposition (EEMD) denoising method for seismic signals," *Energy Procedia*, vol. 97, pp. 84–91, Nov. 2016.

[9] L. Bo, Y. Liming, and L. Dongjie, "Analysis of Longitudinal Vibration Frequency Characteristics of Penetrating Projectile Structure," *Explosion Shock*, vol. 179, no. 3, pp. 208–213, 2018.

[10] M. Perrin, "Hard target fuzing solutions," in *Proc. NDIA 52nd Annu. Fuze Conf.*, 2010.

[11] Y. Jinchuan, L. Dongjie, O. Yangke, and Z. Hui, "The precision control technology of penetration fuze blasting point," *J. Chin. Inertial Technol.*, vol. 24, no. 1, pp. 114–118, 2016.

[12] H. Cao, Y. Zhang, Z. Han, X. Shao, J. Gao, K. Huang, Y. Shi, J. Tang, C. Shen, and J. Liu, "Pole-zero temperature compensation circuit design and experiment for dual-mass MEMS gyroscope bandwidth expansion," *IEEE/ASME Trans. Mechatronics*, vol. 24, no. 2, pp. 677–688, Apr. 2019.

[13] Z. Haifeng, Z. Ya, and L. Shizhong, "Frequency characteristics analysis and overload signal process of penetration projectile," *China Mech. Eng.*, vol. 26, no. 22, pp. 3034–3039, 2015.

[14] M. Sun, X. U. Peng, and D. Shen, "The projectile acceleration processing method using modal analysis and empirical mode decomposition," *J. Detection Control*, 2017.

[15] Y. Zhao, Q. Zhou, and P. Yue "AIP conference proceedings [author(s) advances in energy science and environment engineering," in *Proc. Int. Workshop Adv. in Energy Sci. Environ. Eng. (AESEE)*, Hangzhou, China, vol. 1829, Apr. 2017, Art. no. 020017.

[16] J. Liu, Y. Shi, P. Li, J. Tang, R. Zhao, and H. Zhang, "Experimental study on the package of high-g accelerometer," *Sens. Actuators A, Phys.*, vol. 173, no. 1, pp. 1–8, Jan. 2012.

[17] H. Cao, Y. Zhang, C. Shen, Y. Liu, and X. Wang, "Temperature energy influence compensation for MEMS vibration gyroscope based on RBF NN-GA-KF method," *Shock Vib.*, vol. 2018, Dec. 2018, Art. no. 2830686.

[18] Y. Xiao, Q. Fang, and H. Wu, "A model for rigid sharp–nosed projectile perforating metallic targets considering free–surface and cracking effects," *Explosion Shock Wave*, 2016.

[19] Q. Fang, X. Kong, J. Hong, and H. Wu, "Prediction of projectile penetration and perforation by finite cavity expansion method with the free-surface effect," *Acta Mechanica Solida Sinica*, vol. 27, no. 6, pp. 597–611, Dec. 2014.

[20] Q. Fang and J. Zhang, "3D numerical modeling of projectile penetration into rock-rubble overlays accounting for random distribution of rock-rubble," *Int. J. Impact Eng.*, vol. 63, pp. 118–128, Jan. 2014.

[21] X. Chen, L. Xu, and Q. Zhu, "Mechanical behavior and damage evolution for concrete subjected to multiple impact loading," *KSCE J. Civil Eng.*, vol. 21, no. 6, pp. 2351–2359, Sep. 2017.

[22] T. Gongming, Z. Guoming, and Z. Hualin, "Grid reconstruction method based on LS-PREPOST," China Patent 104 217 082 A, 2014.

[23] H. Cao, Y. Liu, Z. Kou, Y. Zhang, X. Shao, J. Gao, K. Huang, Y. Shi, J. Tang, C. Shen, and J. Liu, "Design, fabrication and experiment of double U-beam MEMS vibration ring gyroscope," *Micromachines*, vol. 10, no. 3, p. 186, 2019.

[24] H. Cao, H. Li, J. Liu, Y. Shi, J. Tang, and C. Shen, "An improved interface and noise analysis of a turning fork microgyroscope structure," *Mech. Syst. Signal Process.*, vols. 70–71, pp. 1209–1220, Mar. 2016.

MIN CUI was born in Dongying, Shandong, China, in 1980. She received the B.S. degree in information countermeasure from the North University of China, Taiyuan, China, in 2002, and the M.S. and Ph.D. degrees in information and communication engineering from the North University of China, in 2005 and 2009, respectively. Since 2005, she has been a Lecturer with the North University of China and the Scientific Researcher with the, Key Laboratory of Shanxi Province, Institute of Signal Capturing and Processing Technology, North University of China. She has authored four articles and holds seven patents. Her research interests are innovative sensing technology and multidimensional signal processing.
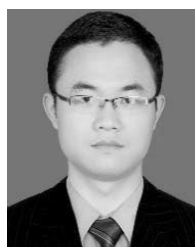
YONG HUANG was born in June 1993, in Lichuan, Hubei, China. He received the bachelor's degree in ground-weapons mobile engineering and the master's degree in instrument engineering from North China University, in 2016 and 2019, respectively. He is currently with the Shanghai Institute of Aerospace Control Technology. His research interests include sensor structure simulation and penetration level algorithm optimization.

JIAN LI was born in Taiyuan, Shanxi, China, in 1985. He received the B.S. degree in information countermeasure and the M.S. and Ph.D. degrees in information and communication engineering from the North University of China, Taiyuan, China, in 2009, 2011, and 2014, respectively. Since 2014, he has been a Lecturer with the North University of China and the Scientific Researcher with the Key Laboratory of Shanxi Province, Institute of Signal Capturing and Processing Technology, North University of China. He has authored eight articles and holds seven patents. His research interests are innovative sensing technology and multidimensional signal processing.

MING MENG was born in Jinzhong, Shanxi, China, in 1992. She received the B.S. degree in 2014 and the bachelor's degree in electronic science and technology from the North University of China, Taiyuan, China, where she is currently pursuing the master's degree with the Department of Applied Mathematics. Her research interests include arrayed inversion reconstruction, cluster analysis, and algorithm optimization.

● ● ●